

# Rough Volatility Project 2025

Flavio Boccia      Ludovico Costa  
Alessandro Pigato    Lorenzo Tolomelli

April 10, 2025

## 1 Estimation of $H$

### 1.1 Simulation of the Lifted Heston variance path

Let us recall that the variance process in the Lifted Heston model is the following:

$$V_t = g_0(t) + \sum_{i=1}^n c_i U_t^i$$

where each factor  $U_t^i$  satisfies the stochastic differential equation

$$dU_t^i = (-x_i U_t^i - \lambda V_t) dt + \nu \sqrt{V_t} dW_t$$

and the Brownian motions driving the price and the variance are correlated according to

$$d\langle B, W \rangle_t = \rho dt.$$

We simulate the variance process in the Lifted Heston model using an implicit-explicit Euler scheme on a uniform time grid. The model assumes that the spot variance  $V_t$  is given by a weighted sum of auxiliary processes  $U_t^i$ , added to a deterministic initial curve  $g_0(t)$ :

$$\widehat{V}_{t_k} = g_0(t_k) + \sum_{i=1}^n c_i \widehat{U}_{t_k}^i, \quad \widehat{U}_0^i = 0.$$

The initial variance curve is defined as:

$$g_0(t) = V_0 + \lambda \theta \sum_{i=1}^n c_i \int_0^t e^{-x_i s} ds,$$

where  $V_0$  is the initial variance level,  $\lambda$  is the mean reversion speed,  $\theta$  is the long-term variance level, and the coefficients  $c_i$  and mean reversion rates  $x_i$  are given by:

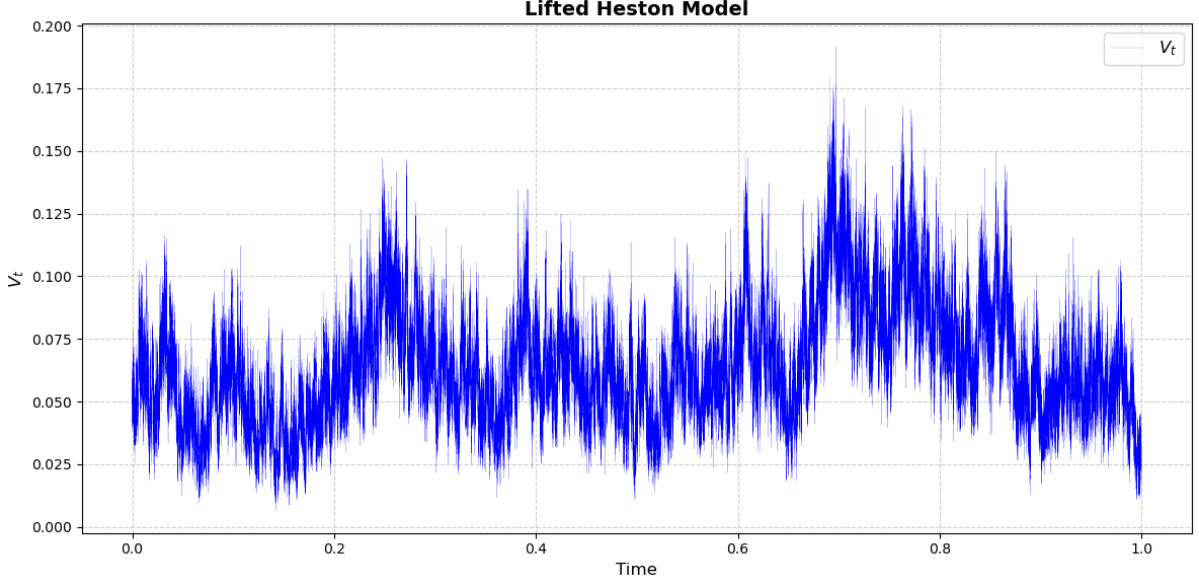
$$c_i = \frac{r^{1-\alpha} - 1}{\Gamma(\alpha)\Gamma(2-\alpha)} \cdot r^{(1-\alpha)(i-1-\frac{n}{2})},$$
$$x_i = \frac{(1-\alpha)(r^{2-\alpha} - 1)}{(2-\alpha)(r^{1-\alpha} - 1)} \cdot r^{i-1-\frac{n}{2}}.$$

The dynamics of each auxiliary process  $\widehat{U}^i$  are simulated using the update:

$$\widehat{U}_{t_{k+1}}^i = \frac{1}{1 + x_i \Delta t} \left( \widehat{U}_{t_k}^i - \lambda \widehat{V}_{t_k} \Delta t + \nu \sqrt{\max(0, \widehat{V}_{t_k})} \Delta W_k \right),$$

where  $\Delta W_k \sim \mathcal{N}(0, \Delta t)$  are Brownian increments.

In the simulation, we use the following parameters:  $n = 20$ ,  $V_0 = 0.05$ ,  $\lambda = 0.3$ ,  $\theta = 0.05$ ,  $\nu = 0.1$ ,  $\alpha = H + 0.5 = 0.6$ ,  $r = r_{20} = 8$ ,  $\Delta t = 10^{-5}$ , and  $m = 10^5$ .



## 1.2 Estimation of $H$ from moments

To estimate the Hurst parameter  $H$ , we follow a two-step regression procedure:

First, for each moment order  $q \in \{0.5, 1, 1.5, 2\}$  and lag  $\Delta \in \{1, \dots, 10\}$ , we compute the empirical moments of the log-variance increments using:

$$m(q, \Delta) = \frac{1}{M_\Delta} \sum_{i=1}^{M_\Delta} |\log(V_{i+\Delta}) - \log(V_i)|^q$$

where  $M_\Delta$  is the number of valid increments of size  $\Delta$ .

Then, for each  $q$ , we fit the following linear regression:

$$\log m(q, \Delta) \approx \zeta_q \log \Delta + C_q$$

The slope  $\zeta_q$  captures the scaling behavior of the process at moment order  $q$ .

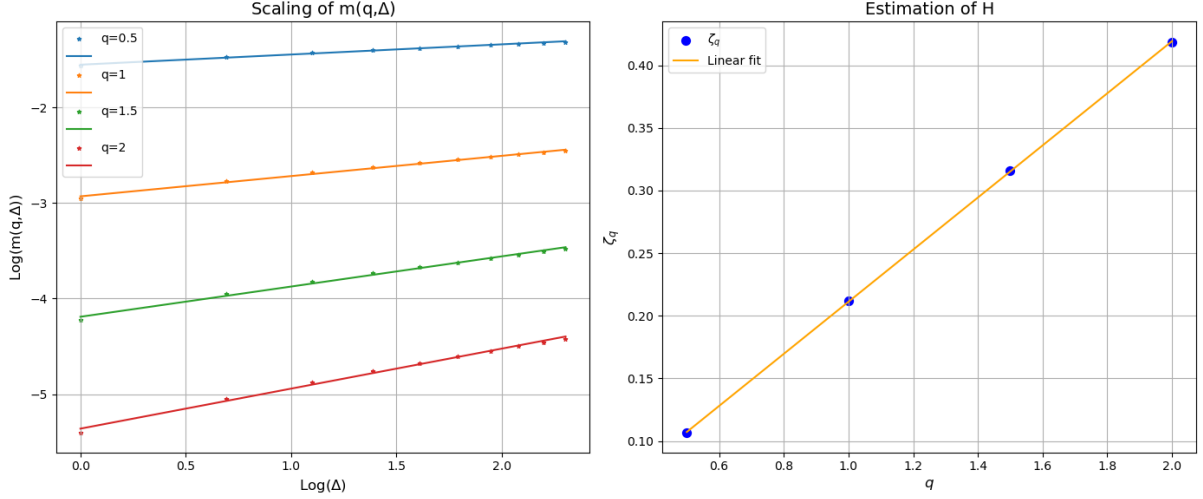
In the second step, we fit another linear regression:

$$\zeta_q \approx H \cdot q + c$$

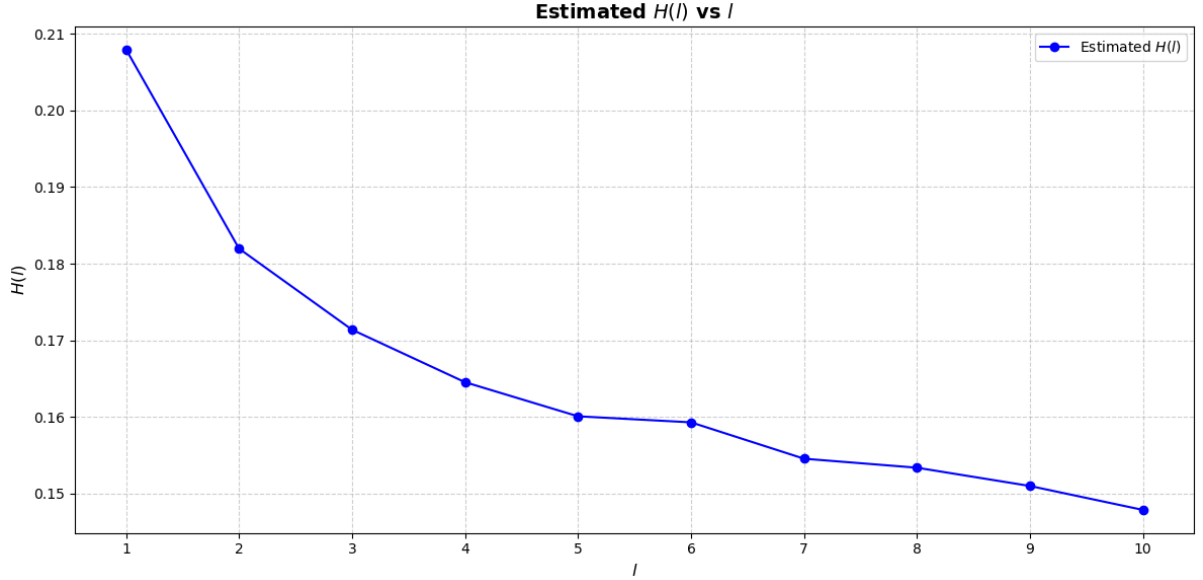
The slope of this fit provides an estimate of the Hurst parameter  $H$ .

Using this method on the simulated path of the Lifted Heston variance, we obtain an estimated value of the Hurst parameter:

$$\hat{H} \approx 0.21$$



### 1.3 Plot of $l$ vs estimated $H(l)$



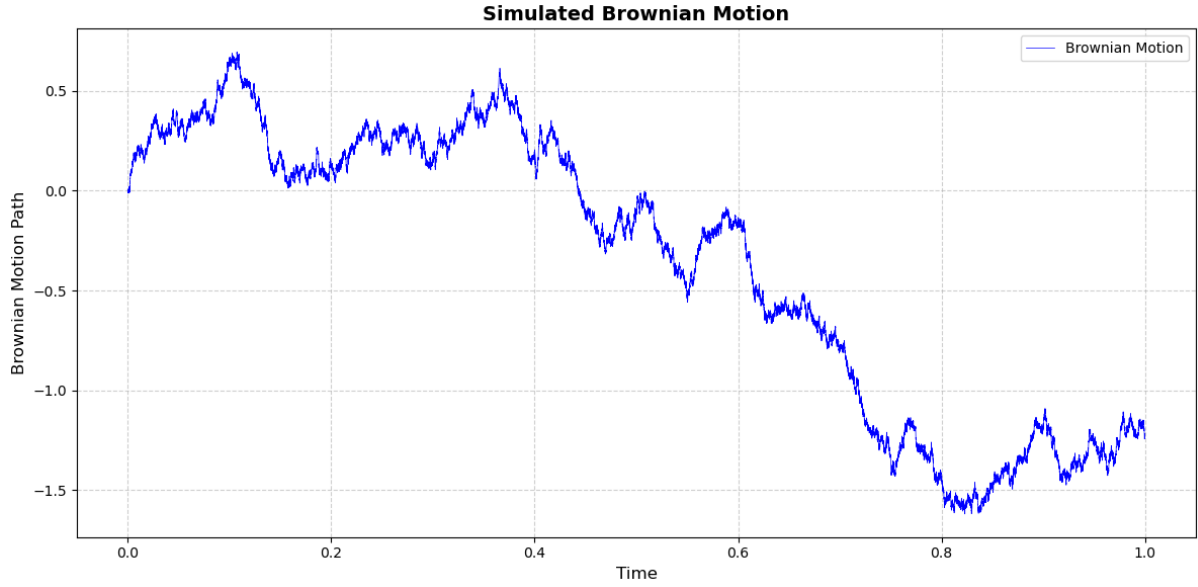
We observe that the estimation of the Hurst parameter  $H(l)$  decreases as the subsampling factor  $l$  increases. As the sampling becomes coarser, the observed process appears rougher, and the estimated Hurst parameter reflects this by tending toward lower values.

### 1.4 Simulation of a Brownian path

A Brownian motion  $W_t$  on the interval  $[0, T]$  can be simulated on a discrete uniform grid  $0 = t_0 < t_1 < \dots < t_m = T$  using its properties of stationary and independent Gaussian increments. Specifically, we set  $W_0 = 0$  and for each  $k = 1, \dots, m$  define:

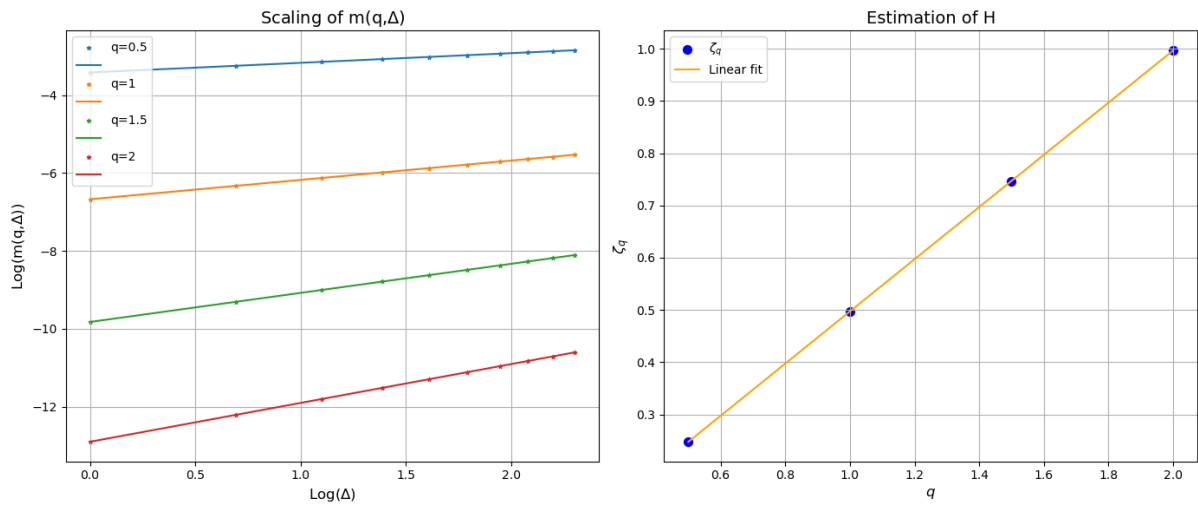
$$W_{t_k} = W_{t_{k-1}} + \sqrt{\Delta t} \cdot Z_k,$$

where  $\Delta t = t_k - t_{k-1}$  is the time step and  $Z_k \sim \mathcal{N}(0, 1)$  are independent standard normal random variables. The result is a discrete-time approximation of the continuous Brownian path.

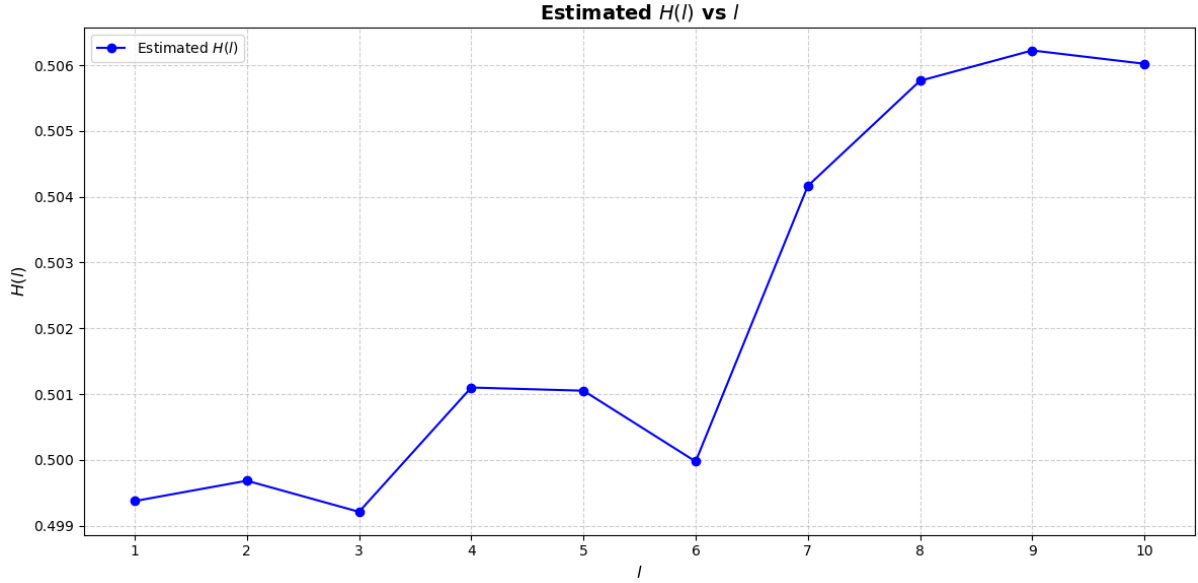


## 1.5 Estimation of $H$ from moments

In this case, we apply the same estimation procedure to a simulated path of a standard Brownian motion. The estimated Hurst parameter is  $\hat{H} \approx 0.50$ , more precisely  $\hat{H} = 0.503$ , which is in excellent agreement with the theoretical value  $H = 0.5$ . This confirms the correctness of the method when applied to a process with known regularity.



## 1.6 Plot of $l$ vs estimated $H(l)$



We observe a slight deterioration in the estimation of the Hurst parameter as  $l$  increases. This behavior is expected, since subsampling reduces the resolution of the data and consequently the accuracy of the estimation. Nonetheless, the estimation remains highly precise, with errors consistently around the order of  $10^{-3}$ , which confirms the robustness of the method when applied to Brownian motion, even with coarser time grids.

## 1.7 Simulation of a fractional Brownian path

Fractional Brownian motion  $W_t^H$  is a continuous Gaussian process with zero mean and covariance function

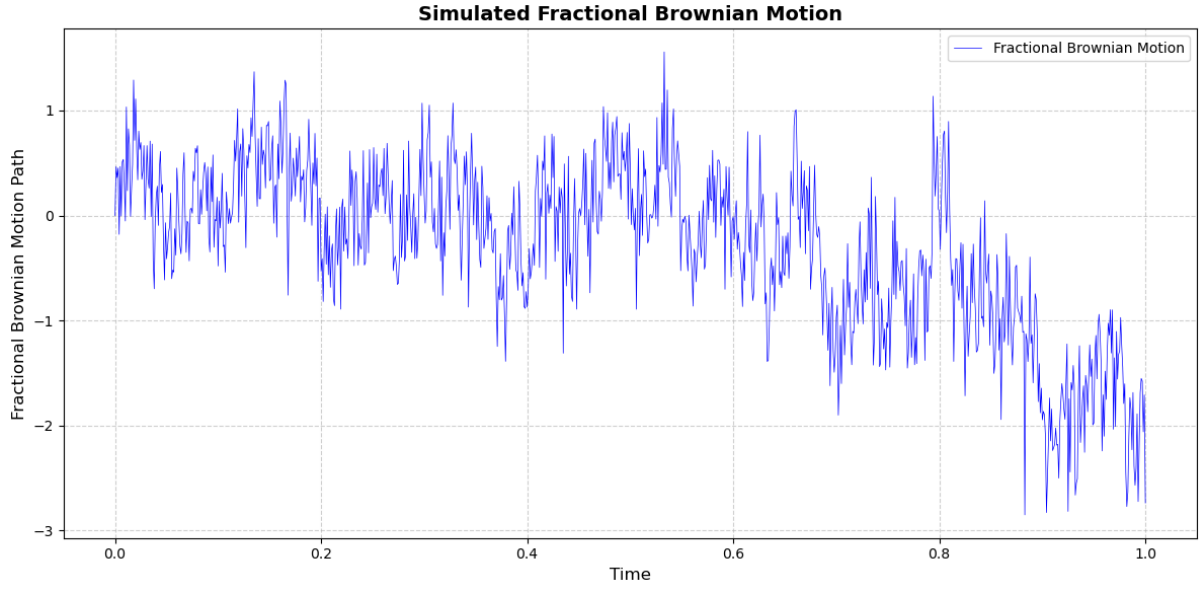
$$\mathbb{E}[W_t^H W_s^H] = \frac{1}{2} (t^{2H} + s^{2H} - |t - s|^{2H}),$$

where  $H \in (0, 1)$  is the Hurst parameter. Unlike standard Brownian motion, fBm has dependent increments: they are positively correlated for  $H > \frac{1}{2}$  and negatively correlated for  $H < \frac{1}{2}$ .

To simulate a fractional Brownian path on a uniform grid  $0 = t_0 < t_1 < \dots < t_m = T$ , we use the Cholesky method:

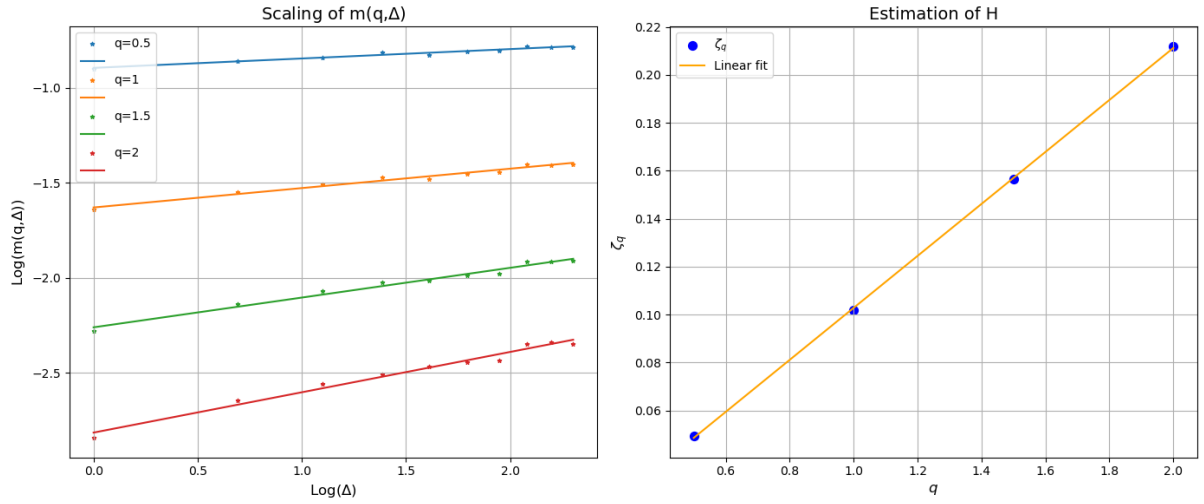
- Build the covariance matrix  $\Sigma$  with entries  $\Sigma_{ij} = \mathbb{E}[W_{t_i}^H W_{t_j}^H]$ .
- Compute its Cholesky decomposition  $\Sigma = CC^\top$ .
- Sample a vector  $Z \in \mathbb{R}^m$  of independent standard normal variables.
- Set  $W^H = CZ$  to obtain the discretized fBm path.

This procedure guarantees exact sampling of the finite-dimensional distribution of the fBm.

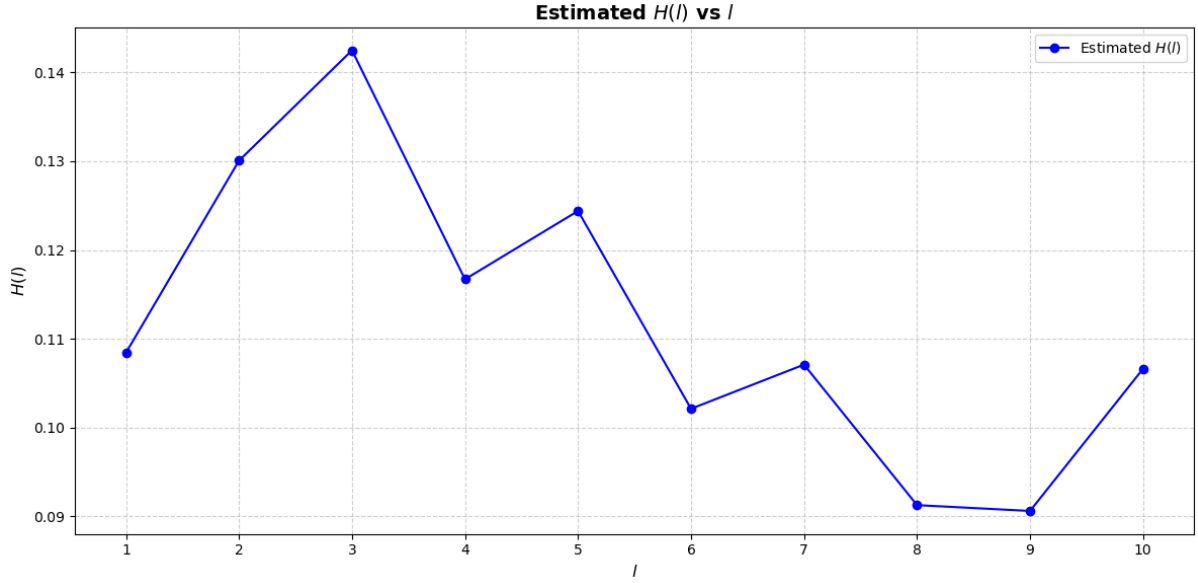


## 1.8 Estimation of $H$ from moments

We apply the same estimation procedure to a simulated path of a fractional Brownian motion with Hurst parameter  $H = 0.1$ . The method yields an estimated value of  $\hat{H} \approx 0.093$ , which is very close to the true value. As in the Brownian motion case, the estimation procedure proves to be accurate and reliable when applied to processes with known regularity.



## 1.9 Plot of $l$ vs estimated $H(l)$



We observe that, similarly to the Brownian motion case, the estimation of the Hurst parameter deteriorates as  $l$  increases. However, the magnitude of the error is larger here: while it remains of order  $10^{-3}$  for Brownian motion, it reaches the order of  $10^{-2}$  for fractional Brownian motion. This suggests that the estimation for very rough processes is more sensitive to subsampling.

## 2 IV Smiles in the Lifted Heston model

### 2.1 Show $M_t$ is a local martingale

$$M_t = \exp \left( u \log(S_t) + \phi(t, T) + \sum_{i=1}^n c_i \psi^i(T - t) U_t^i \right) = \exp(X_t)$$

We begin by computing the differential of the process  $X_t$ :

$$dX_t = d(u \log(S_t)) + d(\phi(t, T)) + d \left( \sum_{i=1}^n c_i \psi^i(T - t) U_t^i \right).$$

To compute the first component, we only need the dynamics of  $S_t$ , which is:

$$dS_t = S_t \sqrt{V_t} dB_t,$$

so that:

$$d(u \log(S_t)) = u \left( \frac{dS_t}{S_t} - \frac{d\langle S \rangle_t}{2S_t^2} \right) = u \left( \sqrt{V_t} dB_t - \frac{V_t}{2} dt \right).$$

To compute the second component, we recall that:

$$\phi(t, T) = \int_0^{T-t} F \left( u, \sum_{j=1}^n c_j \psi^j(s) \right) g_0(T - s) ds,$$

and:

$$d(\phi(t, T)) = -F\left(u, \sum_{j=1}^n c_j \psi^j(T-t)\right) g_0(t) dt = F\left(u, \sum_{j=1}^n c_j \psi^j(T-t)\right) \left(\sum_{i=1}^n c_i U_t^i - V_t\right) dt,$$

where in the last step we used the definition of the variance process:

$$V_t = g_0(t) + \sum_{i=1}^n c_i U_t^i.$$

Finally, let us recall that:

$$\psi^i(t)' = -x_i \psi^i(t) + F\left(u, \sum_{j=1}^n c_j \psi^j(t)\right),$$

$$dU_t^i = (-x_i U_t^i - \lambda V_t) dt + \nu \sqrt{V_t} dW_t,$$

so that the third component is:

$$\begin{aligned} d\left(\sum_{i=1}^n c_i \psi^i(T-t) U_t^i\right) &= \sum_{i=1}^n c_i \left(-\psi^i(T-t)' U_t^i + \psi^i(T-t) dU_t^i\right) \\ &= \sum_{i=1}^n c_i \left[\left(x_i \psi^i(T-t) - F\left(u, \sum_{j=1}^n c_j \psi^j(T-t)\right)\right) U_t^i dt + \psi^i(T-t) dU_t^i\right]. \end{aligned}$$

Putting all together:

$$\begin{aligned} dX_t &= dt \left( -\frac{u}{2} V_t + F\left(u, \sum_{j=1}^n c_j \psi^j(T-t)\right) \left(\sum_{i=1}^n c_i U_t^i - V_t\right) \right. \\ &\quad \left. + \sum_{i=1}^n c_i \left[\left(x_i \psi^i(T-t) - F\left(u, \sum_{j=1}^n c_j \psi^j(T-t)\right)\right) U_t^i + \psi^i(T-t) (-x_i U_t^i - \lambda V_t)\right] \right) \\ &\quad + u \sqrt{V_t} dB_t + \sum_{i=1}^n c_i \psi^i(T-t) \nu \sqrt{V_t} dW_t. \end{aligned}$$

From this we can also compute the quadratic variation of the process  $X_t$ :

$$d\langle X \rangle_t = \left( u^2 V_t + \left( \sum_{i=1}^n c_i \psi^i(T-t) \right)^2 \nu^2 V_t + 2u\nu V_t \rho \sum_{i=1}^n c_i \psi^i(T-t) \right) dt,$$

using the fact that:

$$d\langle B, W \rangle_t = \rho dt.$$

Now, we can compute the differential of  $M_t$ :

$$dM_t = M_t \left( dX_t + \frac{1}{2} \langle X \rangle_t \right),$$

and to show that  $M_t$  is a local martingale we just need to show that it has zero drift.



The drift is equal to:

$$\begin{aligned}
& -\frac{u}{2}V_t + F\left(u, \sum_{j=1}^n c_j \psi^j(T-t)\right) \sum_{i=1}^n c_i U_t^i - V_t F\left(u, \sum_{j=1}^n c_j \psi^j(T-t)\right) + \sum_{i=1}^n c_i x_i \psi^i(T-t) U_t^i \\
& - F\left(u, \sum_{j=1}^n c_j \psi^j(T-t)\right) \sum_{i=1}^n c_i U_t^i - \sum_{i=1}^n c_i x_i \psi^i(T-t) U_t^i - \sum_{i=1}^n c_i \psi^i(T-t) \lambda V_t \\
& + \frac{u^2}{2}V_t + \left(\sum_{i=1}^n c_i \psi^i(T-t)\right)^2 \nu^2 \frac{V_t}{2} + u\nu V_t \rho \sum_{i=1}^n c_i \psi^i(T-t),
\end{aligned}$$

where the terms in blue and red directly cancel each other. The terms in orange are:

$$V_t \left( \frac{1}{2}(u^2 - u) + (\rho\nu u - \lambda) \sum_{j=1}^n c_j \psi^j(T-t) + \frac{\nu^2}{2} \left( \sum_{j=1}^n c_j \psi^j(T-t) \right)^2 \right),$$

which become:

$$V_t F\left(u, \sum_{j=1}^n c_j \psi^j(T-t)\right),$$

since:

$$F(u, v) = \frac{1}{2}(u^2 - u) + (\rho\nu u - \lambda)v + \frac{\nu^2}{2}v^2,$$

and we can easily see that the the drift goes to zero.

To conclude, we observe that if  $M_t$  is a true martingale, then it satisfies

$$M_t = \mathbb{E}[\exp(u \log S_T) | \mathcal{F}_t].$$

Indeed, using the martingale property, we have the following:

$$\mathbb{E}[M_T | \mathcal{F}_t] = M_t,$$

and

$$M_T = \exp\left(u \log(S_T) + \phi(T, T) + \sum_{i=1}^n c_i \psi^i(0) U_t^i\right) = \exp(u \log(S_T)),$$

where we use that  $\phi^i(0) = 0$  and  $\phi(T, T) = 0$ .

## 2.2 Carr-Madan Formula

Let  $X_t = \log S_t$  and  $\hat{q}$  be the characteristic function, i.e. the Fourier transform, of the density function  $q$  of  $X_T$  then:

$$\hat{q}(u) = \mathbb{E}[e^{iu \log S_T}].$$

For a derivative with payoff  $f(X_T)$  we have that its price can be written as follows:

$$C_0 = \frac{e^{-rT}}{2\pi} \int_{\mathbb{R}} \hat{f}(u + iw) \bar{\hat{q}}(u + iw) du.$$

The first term in the integral represents the Fourier transform of the payoff function, expressed in terms of the log-price variable  $X_T$ . The payoff function is given by:

$$f(x) = (e^x - K)^+.$$

Therefore, its Fourier transform, evaluated at a complex argument  $u + iw$ , is:

$$\hat{f}(u + iw) = \int_{\mathbb{R}} e^{i(u+iw)x} (e^x - K)^+ dx.$$

Now we can see that:

$$\begin{aligned} \hat{f}(u + iw) &= \int_{\log K}^{+\infty} e^{(1+i(u+iw))x} dx - K \int_{\log K}^{+\infty} e^{i(u+iw)x} dx \quad \text{support of the payoff is } x \geq \log K \\ &= -\frac{e^{(i(u+iw)+1)\log K}}{i(u+iw)+1} + K \frac{e^{i(u+iw)\log K}}{i(u+iw)} \quad \text{the two integrals converge for } w > 1 \\ &= \frac{e^{(i(u+iw)+1)\log K}}{(1+i(u+iw))(i(u+iw))} \quad \text{adding similar terms together} \end{aligned}$$

Now, let us consider  $w = 1 + \alpha_2, \alpha_2 > 0$ :

$$1 + i(u + iw) = iu - \alpha_2,$$

$$iu - w = iu - 1 - \alpha_2,$$

so that:

$$\hat{f}(u + i(1 + \alpha_2)) = \frac{e^{(iu - \alpha_2)\log K}}{(iu - 1 - \alpha_2)(iu - \alpha_2)}.$$

For the second term we need the following:

$$\bar{\hat{q}}(u + iw) = \mathbb{E}[e^{-i(u+iw)\log S_T}] = \mathbb{E}[e^{i(-u-iw)\log(S_T)}],$$

and considering again  $w = 1 + \alpha_2, \alpha_2 > 0$  we obtain:

$$\bar{\hat{q}}(u + i(1 + \alpha_2)) = \mathbb{E}[e^{i(-u-i(1+\alpha_2))\log(S_T)}] = \Phi(-u - (1 + \alpha_2)i).$$

Putting all together we obtain:

$$\begin{aligned} C_0 &= \frac{e^{-rT}}{2\pi} \int_{\mathbb{R}} \frac{e^{(iu - \alpha_2)\log K}}{(iu - 1 - \alpha_2)(iu - \alpha_2)} \Phi(-u - (1 + \alpha_2)i) du \\ &= \frac{e^{-rT - \alpha_2 \log K}}{2\pi} \int_{\mathbb{R}} \frac{e^{iu \log K}}{(iu - 1 - \alpha_2)(iu - \alpha_2)} \Phi(-u - (1 + \alpha_2)i) du \\ &= \frac{e^{-rT - \alpha_2 \log K}}{2\pi} \int_{\mathbb{R}} \frac{e^{-iu \log K}}{(iu + 1 + \alpha_2)(iu + \alpha_2)} \Phi(u - (1 + \alpha_2)i) du \end{aligned}$$

where in the last equality we use the change of variable

$$\tilde{u} = -u.$$

Now, we can use the following proposition:

**Proposition 1** *Let  $f : \mathbb{R} \rightarrow \mathbb{C}$  be a complex-valued function such that*

$$f(-u) = \overline{f(u)} \quad \text{for all } u \in \mathbb{R}.$$

*Then,*

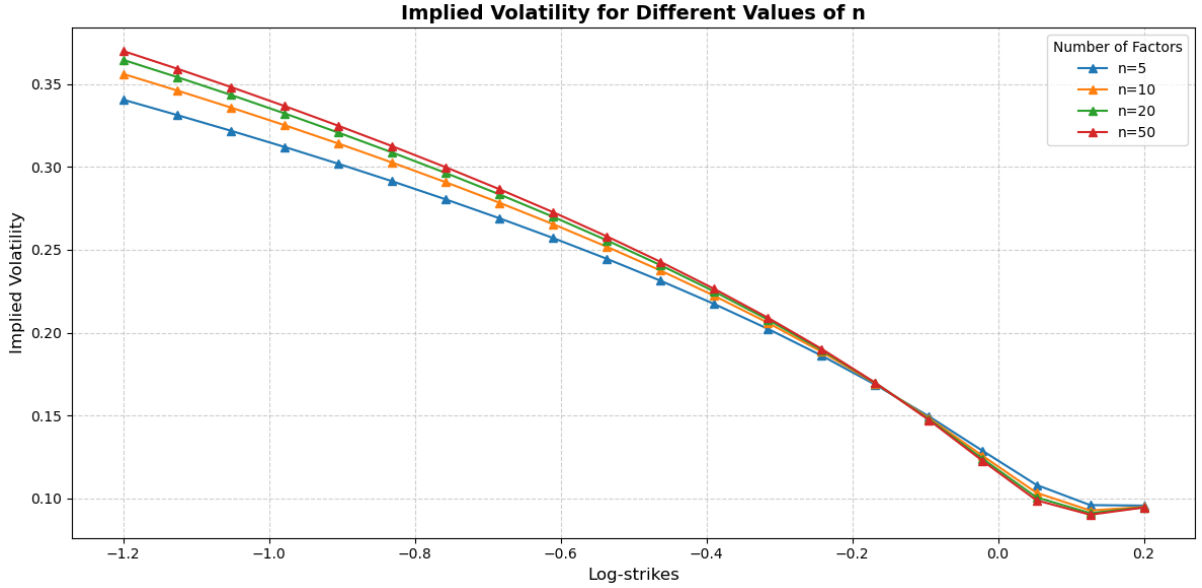
$$\int_{-\infty}^{\infty} f(u) du = 2 \int_0^{\infty} \operatorname{Re}(f(u)) du.$$

It is easy to see that the condition  $f(-u) = \overline{f(u)}$  holds in our case, so that, finally:

$$C_0 = \frac{e^{-rT}}{\pi} \int_0^{+\infty} \operatorname{Re} \left[ \frac{\Phi(u - (1 + \alpha_2)i)}{(iu + 1 + \alpha_2)(iu + \alpha_2)} e^{-iu \log K} \right] du$$

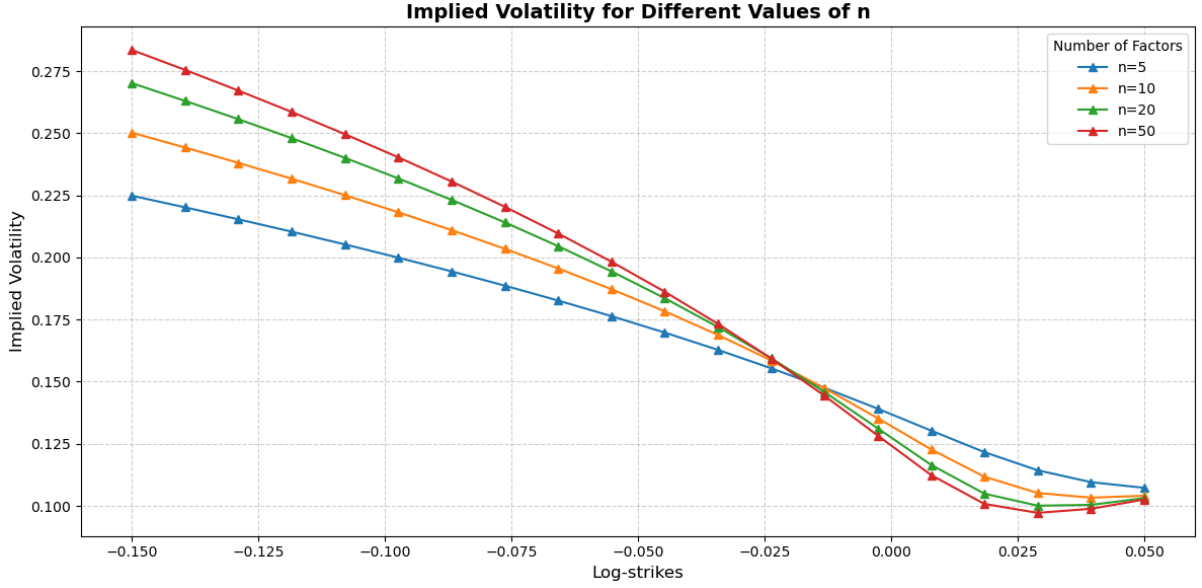
## 2.5 IV Smiles in the Lifted Heston model

Here we show the implied volatility smile for  $T = 1$ , using truncation level  $L = 100$ , for different values of  $n$  in the Lifted Heston model.



The plot shows the implied volatility smiles generated by the Lifted Heston model for different values of the number of factors  $n$ . We observe that increasing  $n$  leads to a steeper and more pronounced smile, particularly on the left wing. This reflects the improved ability of the model to approximate the rough volatility kernel with more factors. While the differences between  $n = 5$  and  $n = 20$  are significant, the curves for  $n = 20$  and  $n = 50$  are almost indistinguishable, indicating that the approximation has converged. This illustrates the trade-off between computational cost and accuracy when choosing the number of factors in practical implementations.

Here we show the implied volatility smile for  $T = 1$ , using truncation level  $L = 1000$ , for different values of  $n$  in the Lifted Heston model.

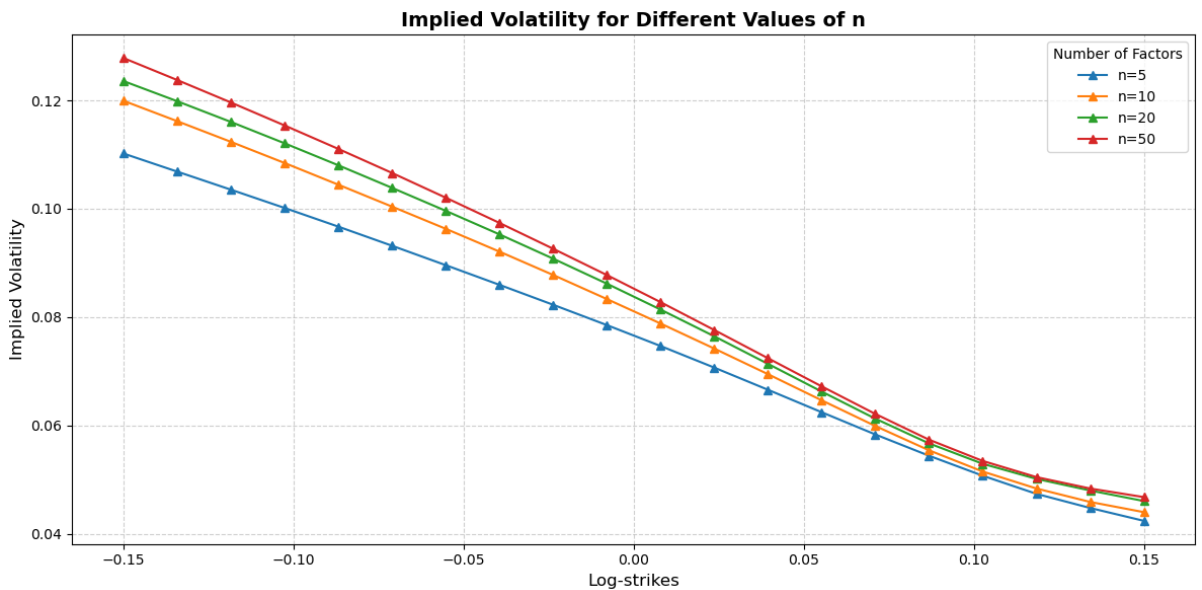


The plot shows the implied volatility smile for maturity  $T = \frac{1}{26}$ , computed using truncation level  $L = 1000$ , for different values of  $n$  in the Lifted Heston model. As in the long-maturity case, increasing  $n$  enhances the model's ability to capture the steepness of the smile. However, the differences between curves are more pronounced here, especially on the left wing, where low strikes exhibit sharper skews for higher  $n$ . This reflects the higher sensitivity of short-term options to the fine structure of volatility, which the multi-factor approximation improves by increasing the number of factors.

### 3 Lifted Bergomi IV Smile

#### 3.3 IV Smile in the Lifted Bergomi model

We display the implied volatility smile for  $T = 1$ , with option prices computed using a Monte Carlo method based on  $N = 100000$  simulations.



The plot shows the implied volatility smile for maturity  $T = 1$ , for different values of  $n$  in the Lifted Bergomi model. As in the Lifted Heston case, increasing  $n$  improves the model's capacity to reproduce the observed steepness of the smile. The effect is particularly noticeable for negative log-strikes, where larger  $n$  leads to sharper skews, better aligning with market behavior.

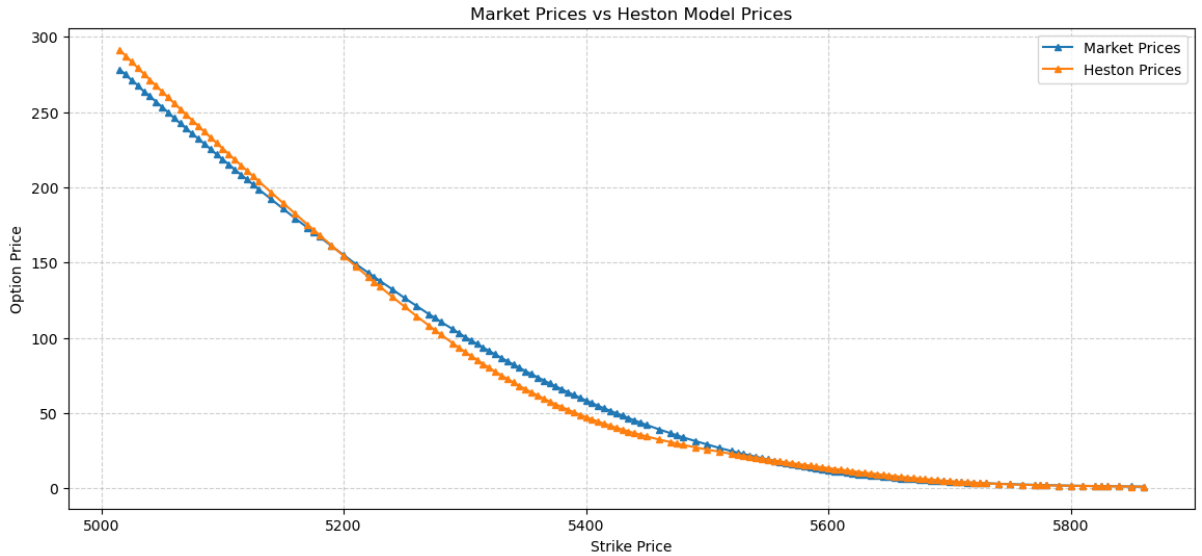
## 4 Calibration of Heston and Lifted Heston models

In this section, we perform a calibration of the classical Heston model and the Lifted Heston model to a dataset consisting of approximately 150 SPX call options with a two-weeks maturity. The aim is to assess and compare the ability of these models to fit market data, both in terms of prices and implied volatilities.

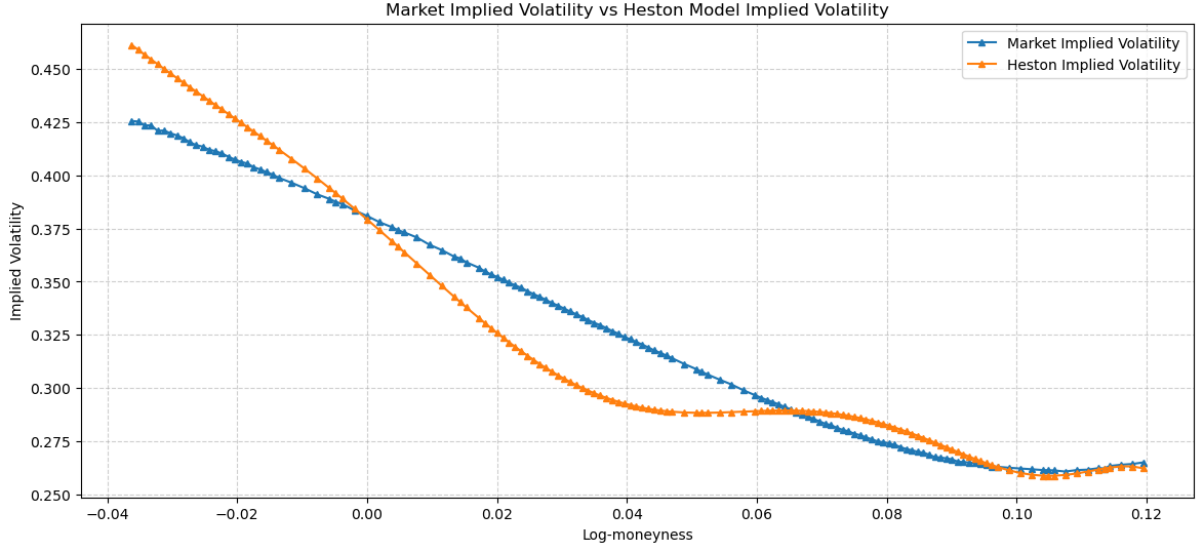
Given the additional flexibility provided by the multiple factors in the Lifted Heston model, we expect a significant improvement in calibration quality compared to the standard Heston model. However, this enhancement comes at the cost of increased computational time due to the higher model complexity and the numerical solution of the Riccati system.

### 4.1 Heston Model

The calibration of the Heston model is performed with a tolerance of  $10^{-15}$ . The computational efficiency of the calibration is mainly due to the analytical tractability of the model, which enables a fast evaluation of option prices through its explicit characteristic function and Fourier-based pricing methods.



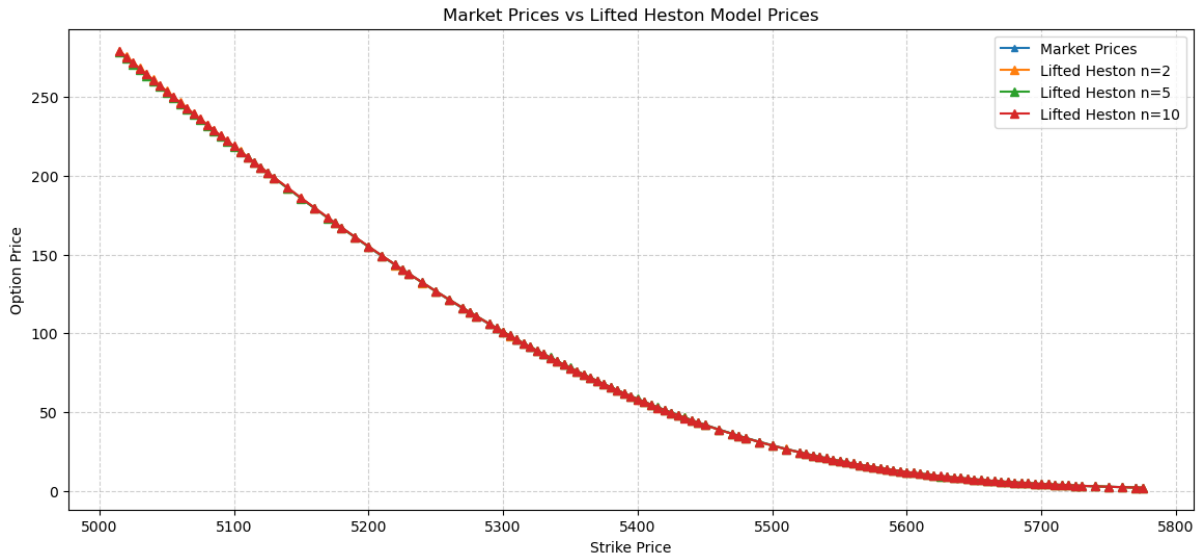
The plot shows the comparison between market prices (in blue) and the prices obtained from the Heston model (in orange). The calibration yields a very good fit across the range of strikes, with model prices closely tracking the observed market data.



The plot displays the implied volatilities derived from market prices (blue) and those obtained from the Heston model (orange). While the calibration does not fully capture the shape of the implied volatility smile—particularly the oscillations visible in the model curve—it is nonetheless promising. The model successfully captures the overall trend of the market volatility structure. We expect these oscillations to be significantly reduced in the Lifted Heston model, which offers greater flexibility.

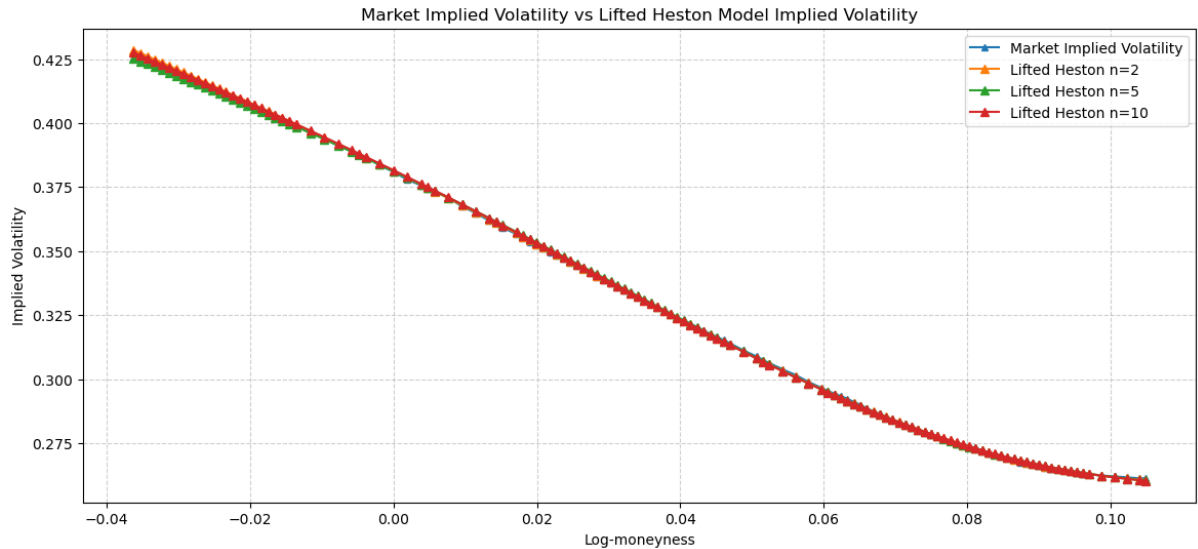
## 4.1 Lifted Heston Model

For the calibration of the Lifted Heston model, we reduced the tolerance to  $10^{-6}$  in order to mitigate the computational time. As expected, the computational complexity increases with respect to the classical Heston model, due to the higher dimensionality introduced by the additional factors. In the following, we perform the calibration for  $n = 2, 5, 10$  factors. The remaining parameters of the model have been fixed to the following values:  $\alpha = 0.7$ ,  $\alpha_2 = 1$ ,  $M = 100$ ,  $L = 100$ .



The plot shows the comparison between market data and the prices obtained from the Lifted Heston model. We observe that there is no noticeable difference between the

models calibrated with  $n = 2, 5, 10$  factors. The prices produced by the Lifted Heston model for different values of  $n$  almost perfectly overlap and match the market prices across all strikes. This confirms the robustness of the model with respect to the choice of  $n$ , and shows that even a small number of factors is sufficient to achieve a good calibration. Moreover, the Lifted Heston model provides an improvement over the classical Heston model, particularly in capturing the shape of the smile for short maturities.



The plot shows the implied volatilities from market data and the Lifted Heston model. We observe that the Lifted Heston model provides a very good fit to the market implied volatility surface. The results obtained with  $n = 2, 5, 10$  factors are almost indistinguishable, indicating that increasing the number of factors has a limited impact on the quality of the fit in this case. The model is able to capture both the level and the slope of the market smile, significantly improving the calibration compared to the classical Heston model, which is known to struggle especially for short maturities or steep smiles.